A Triboelectric Piston-Cylinder Assembly with Condition Monitoring and Self-powering Capabilities

Guoxing Li, Hongyu Wu, Rui Guo, Hulin Zhang*, Lintao Li, Muhammad Yousaf Iqbal, Fengshou Gu*

G. Li, H. Wu, L. Li, M. Y. Iqbal,
Department of Vehicle Engineering, Taiyuan University of Technology, Taiyuan, 030024, China
E-mail: liguoxing@tyut.edu.cn

R. Guo, H. Zhang,
Micro Nano System Research Center, College of Information and Computer, Taiyuan University of Technology, Taiyuan, 030024, China
E-mail: zhanghulin@tyut.edu.cn

F. Gu
Center for Efficiency and Performance Engineering, University of Huddersfield HD1 3DH, UK

Keywords: triboelectric nanogenerator, piston-cylinder assembly, reciprocating machinery, condition monitoring, self-powering

Abstract: The condition monitoring of piston-cylinder reciprocating machinery usually relies on vibration and acoustic sensors installed on the outer surface of cylinders. However, vibration and acoustic signals are susceptible to external interference from other accessories, and require an external power supply, which limits its widespread application. Based on the lateral sliding mode of triboelectric nanogenerator (TENG), this paper proposes a novel reciprocating device with condition monitoring and self-powering capabilities, called piston-cylinder triboelectric nanogenerator (PCTN). The effects of different factors, including mean piston speed, number of piston rings, materials of piston ring and cylinder, on the output characteristics of PCTN are investigated respectively. Two typical fault cases, i.e., piston ring missing and coil fracture, are investigated to verify the condition monitoring capability of PCTN. Piston ring missing faults can be effectively identified based on the variations in peak and RMS values of short-circuit

current (I_{sc}). Coil fracture faults can be identified and located by analyzing changes in time-domain curve and time-frequency spectrum of I_{sc}. This paper provides a theoretical and experimental basis for the widespread application of PCTN in reciprocating machinery.

1. Introduction

The piston-cylinder reciprocating structure is widely used in various mechanical systems, such as reciprocating air compressors, internal combustion engines, hydraulic actuators, etc. The condition monitoring and fault diagnosis of reciprocating assemblies are of great significance to the operation and maintenance of mechanical systems. Since reciprocating assemblies are often directly in contact with coolant, hydraulic oil and high-pressure gas, conventional sensors cannot be installed inside the cylinder. For this reason, some scholars installed vibration and acoustic sensors on the outer surface of structure to implement non-intrusive condition monitoring.[1–3] By analyzing measured data, online condition monitoring and early fault identification of reciprocating components can be realized. However, vibration and acoustic signals are susceptible to external interference from other accessories, introducing errors and affecting diagnostic accuracy. Moreover, the sensor requires an external power supply, which increases the complexity of the structure, the difficulty of monitoring and the cost of operation.

The first concept of triboelectric nanogenerator (TENG) proposed by Prof. Wang in 2012, was a disruptive technology after that world attracted wide attention.[4–6] The TENG is a device based on the conjunction of triboelectrification and electrostatic induction to convert mechanical energy into electrical energy through contact-separation or relative sliding between two materials with opposite frictional polarities.[7] TENG has four working modes, respectively: vertical contact-separation mode,[8-9] lateral sliding mode,[10–13] single-electrode mode[14] and freestanding triboelectric-layer mode.[15-16] TENG has so many advantages such as self-powering, diverse structure, low cost, high energy conversion efficiency[17] and high energy density.[18-19] So it is widely used in small power supply equipment (using water wave energy,[19-20] human motion,[21] etc. to collect energy) and self-powered active sensor devices (displacement sensors,[22] acceleration sensors,[23–25] dynamic wear sensors,[26] wind speed and direction sensors,[27-28] pressure sensors,[29-30] healthcare sensing,[31] etc.). Small power supply equipment can be used to power traditional sensors or other devices by harvesting energy from the environment. While the self-powered active sensor can actively generate electrical signals, from which the state of the surrounding environment can be obtained to realize the function of the sensor. Jing et al. designed a cased-encapsulated triboelectric nanogenerator (cTENG) based

on sliding electrification that can convert reciprocating motion into electrical energy and address environmental vibration motions of large amplitude and low frequency.[10] Zhu et al. developed a new principle for harvesting energy from different mechanical motions (contacted sliding, lateral translation and rotation/rolling) based on TENG of the fully contacted, sliding electrification process.[11] This is a structure similar to a grating and two gratings are of the same size to fit each other. But during the sliding process, the contact area will gradually decrease. Both the contact area and sliding speed can affect its power generation capacity. Therefore, it is difficult to distinguish a specific factor that causes the change in power generation capacity. If the area of one of the gratings is reduced, the contact area between them will remain unchanged during the entire sliding process.

Based on the lateral sliding mode of TENG, this paper proposes a novel reciprocating device with condition monitoring and self-powering capabilities, called piston-cylinder triboelectric nanogenerator (PCTN). The differences between PCTN and ordinary piston-cylinder structures are as follows: two sets of interdigital electrodes are pasted on the outer wall of the cylinder, and multiple coils are distributed on the interdigital electrode. The piston adopts a modular design, the number of piston rings can be changed by changing the number of piston heads. The effects of different factors, including mean piston speed, number of piston rings, materials of piston ring and cylinder, on the output characteristics of PCTN are investigated respectively. Two typical fault cases, i.e., piston ring missing and coil fracture, are investigated to verify the condition monitoring capability of PCTN. This paper provides a theoretical and experimental basis for the widespread application of PCTN in reciprocating machinery.

2. Results and discussion

2.1. Structure of the PCTN

As shown in **Figure 1**(a), PCTN adopts a piston-cylinder structure consisting of four parts: cylinder, piston, interdigital electrode, and connecting rod. A photograph of the PCTN is shown in Figure 1(b). The interdigital electrodes are composed of two groups and pasted on the outer wall of the cylinder which are made of Polymethyl methacrylate (PMMA). Figure 1(c) shows the unfolding shape of two sets of interdigital electrodes, the coils on the two sets of electrodes are arranged alternately. The crank connecting rod mechanism converts the input rotary motion by the external drive (motor) into the reciprocating linear motion of the piston. The piston is composed of a piston base, several detachable piston heads and piston rings, wherein the piston base is threadedly connected with a connecting rod. The piston head adopts a modular design so that multiple piston heads can be connected in series. A ring groove is arranged between the

contact surfaces of the piston head and the piston base or adjacent piston head for installing the piston ring. The advantage of this modular design is that the number of piston rings can be changed by increasing or decreasing the number of piston heads. Figure 1(d) shows the assembly diagram of the piston heads and piston rings. The piston ring is made of polyformaldehyde (POM). In order to ensure the sealing of the moving pairs, the piston ring should be closely attached to the inner surface of cylinder driving by its own elasticity. Before the piston is installed in the cylinder, the diameter of the piston ring (D_R) is greater than the inner diameter of the cylinder (D_C). The distance between two piston rings can be adjusted by changing piston heads with different height (b_B). The piston ring has a certain degree of floatability in the axial direction, which is achieved by matching the piston ring height (b_R) with the ring groove width. The distance between adjacent coils (B_C) on the interdigital electrode and the width of one coil (B_E) should match the height of piston head (b_B) and the piston ring height (b_R), which is $B_C + B_E = b_B + b_R$ to optimize the generation of electrical energy. Detailed dimensions are presented in Supplementary **Table S1**.

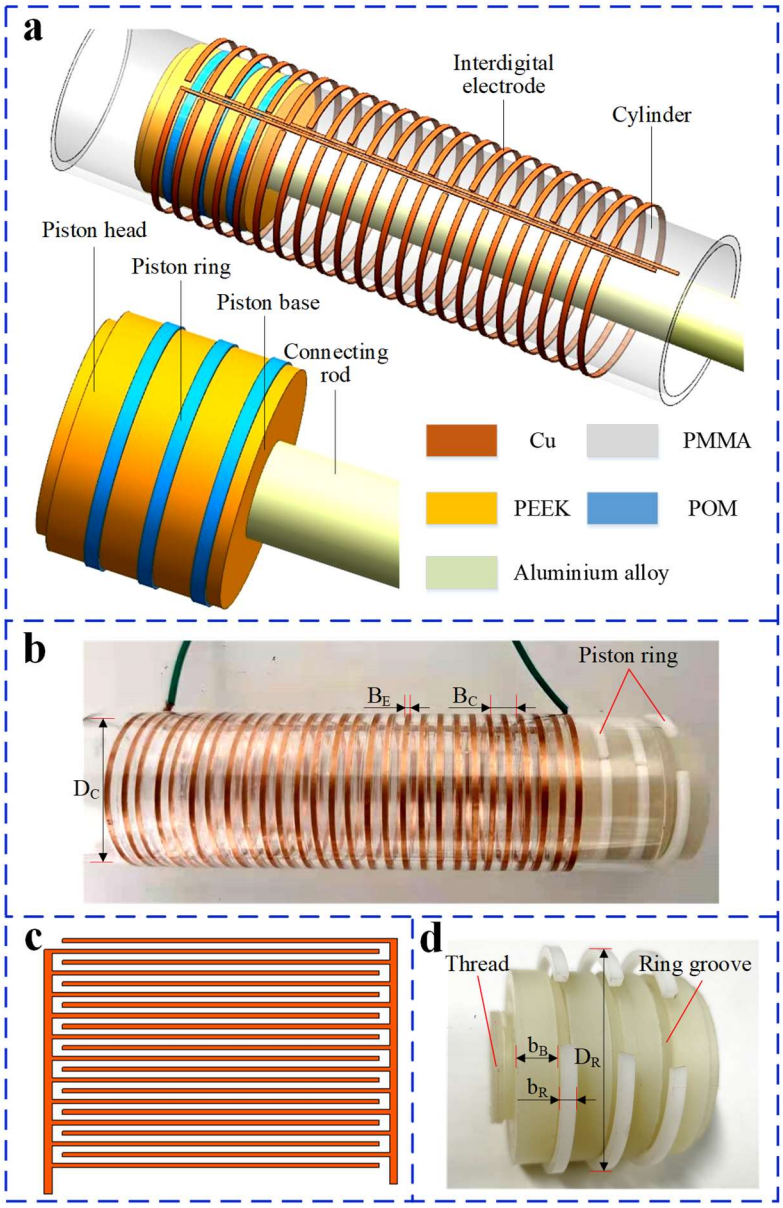

Figure 1. Structure design of PCTN based on lateral sliding mode TENG: (a) Schematic illustrations of PCTN (b) photograph of the PCTN, (c) interdigital electrode expanded drawing and (d) photograph of the piston assembly.

2.2. Working principle of the PCTN

Based on the conjugation of the triboelectric effect and electrostatic induction, the relative sliding between two materials with opposite tribo-polarity will cause charge transfer to form a potential difference between two electrodes attached on the outer surface of the cylinder. Driven by this potential difference, electrons flow between the two electrodes through an external circuit.[7]

Figure 2(a) shows the schematic diagram of the electricity generation process of the designed PCTN. The first electrode close to the piston ring is defined as electrode A, marked

in red; and the electrode which is next to electrode A is defined as electrode B, marked in orange. In the first stage (i), when the POM ring, marked in blue, slides to a position that fully overlaps with electrode A, equal amounts of charges are generated on the top surface of the POM ring and on the surface of the PMMA cylinder. Then, the positive charges in the external circuit will be attracted to the surface of electrode A and the negative charges will be attracted to the electrode B due to electrostatic induction. In the second stage (ii), as the ring moves toward electrode B, the negative charges will flow from electrode B to electrode A via the external load to screen the local electric field of non-moving positive charges on the cylinder. In the third stage (iii), when the ring slides to the position overlapping with electrode B, all of the negative charges are driven to electrode A, completing the half-cycle of electricity generation process. In the fourth stage (iv), as the ring slides toward to the next adjacent electrode A, negative charges will flow from electrode A to electrode B, forming a current opposite to the second stage in the external circuit. After that, the ring continues to slide until it overlaps with electrode A. This is the second half-cycle of the electricity generation process. Obviously, with the reciprocating movement of the piston, the periodic repetition of four stages (stage i to stage iv) generates an alternating current in the external circuit.

In the open-circuit condition, electrons cannot be transferred between the two electrodes as there is no external load. We define the open-circuit voltage (V_{oc}) as the potential difference between the two electrodes. As shown in the middle inset of Figure 2(a), the maximum V_{oc} appears at stage i and stage iii when the negative charges completely screen the positive charges on one of the electrodes. The distributions diagram of V_{oc} at the four stages obtained by finite-element simulation, as shown in Figure 2(b). The simulated potential distribution is in good agreement with the schematic diagram, which further clarifies the working principle.

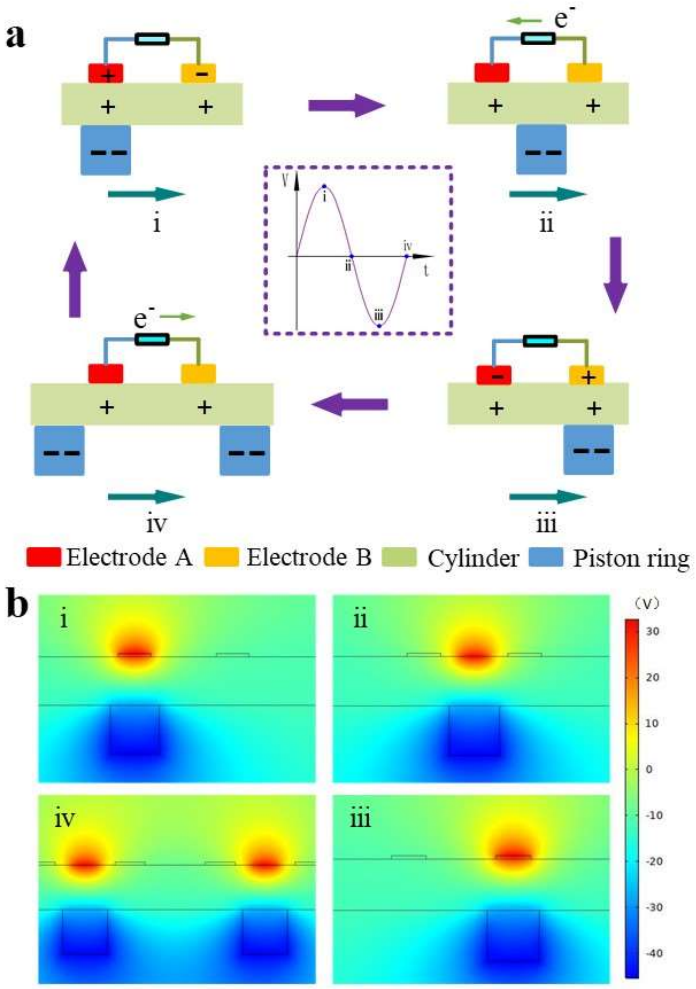

Figure 2. (a) Schematic working principle of PCTN (i-iv), the middle illustration shows the variation in open-circuit voltage with time, (b) the simulated potential distributions of the piston ring at four different positions employing the finite element simulation method (i-iv).

2.3. Output characteristics of the PCTN

To characterize the electrical output performance of the PCTN, a motor driven piston-cylinder reciprocating system with adjustable rotating speed controlled by a frequency converter is established. Photographs of the experimental facility are presented in Supplementary **Figure S1**(a), and experimental video is shown in Supplementary **Video S1**. It can be seen that as the motor rotating speed increases, the frequency of the light-emitting diode (LED) bulbs flickering becomes higher, which has excellent self-powering capacity. And the LED bulbs are brighter at a motor speed of 254 r min^{-1} than at 100 r min^{-1} (Supplementary **Figure S1**(b, c). If a capacitor (10 μF) is connected in parallel behind the rectifier bridge to store charges, the PCTN can achieve stable power output (Supplementary **Video S2**) which has an excellent self-powering capability.

Then, the output characteristics of PCTN equipped with three piston rings under different piston speeds are analyzed. Since the piston speed changes periodically, the speed condition of PCTN is marked with the mean piston speed, referred to as v_m. The output signals of the short-circuit current (I_{sc}) and the open-circuit voltage (V_{oc}) are measured respectively at different v_m. **Figure 3**(a) shows that as v_m increases from 0.12 to 0.6 m s^{-1}, the peak value of short-circuit current (I_{sc}) increases from 0.4uA to 2.46μA, which is proportional to the v_m. As shown in Figure 3(b), V_{oc} remains almost constant and the peak-to-peak values are about 40 V when the v_m increases from 0.36 to 0.6 m s^{-1}. But the value of V_{oc} at the v_m of 0.12 and 0.24 m s^{-1} is lower than that of other v_m. This may be attributed to the partial contact of piston rings with the inner wall of cylinder caused by gravity and other dynamic interferences under low-speed conditions, resulting in a reduction in the effective contact area. And the environmental noise will also have an impact on the PCTN at a low speed. Wang et al.[27] and Han et al. [32] showed a similar phenomenon in their experiments. In fact, at the two ends of each stroke, the decrease in the sliding speed of the piston will cause a reduction in the V_{oc} amplitude, resulting in a sine wave-like profile for the envelope of V_{oc} in each stroke.

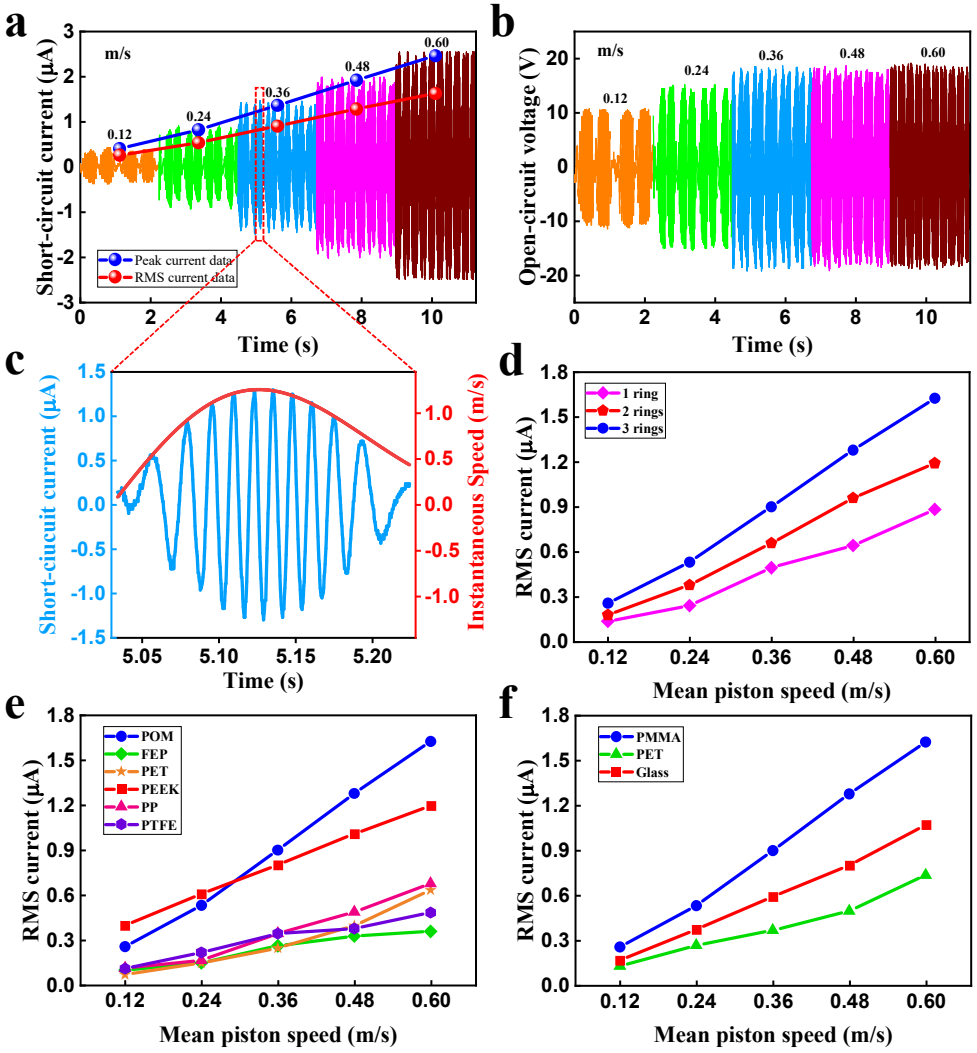

Figure 3. Electrical output measurements of the PCTN: (a) I_{sc} and (b) V_{oc} at different mean piston speeds, (c) comparison of I_{sc} and piston instantaneous speed, RMS value of I_{sc} with (d) different numbers of rings, (e) different ring materials, and (f) different cylindrical materials.

According to the theory of the triboelectric nanogenerator, the two interdigital electrodes of PCTN can be regarded as a capacitor that transfer charges Q between the electrodes. Since the arrangement of the electrodes remains unchanged, the capacitance is almost constant. Thus, according to Equation 1:

$$C = \frac{Q}{V_{oc}} \tag{1}$$

the V_{oc} is linearly related to the constant charges Q transferred between the two electrodes, which depends on the contact area between piston rings and the inner wall of the cylinder. However, both the peak and the root mean square (RMS) values of the I_{sc} will vary linearly as the changes of v_m, which are regarded as the key characteristic parameters of PCTN. The I_{sc} could be derived as Equation 2:

$$I_{sc} = \frac{dQ}{dt} = \frac{dQ}{dx}\frac{dx}{dt} = \frac{dQ}{dx}v_p \quad (2)$$

where $\frac{dQ}{dx}$ is the charge change rate, which is a constant dependent on the inherent parameters of PCTN. Therefore, the I_{sc} is linearly related to the instantaneous piston speed v_p. As shown in Figure 3(c), the envelope curve of I_{sc} peaks is in good agreement with the instantaneous piston speed. When the piston moves from one end of the cylinder to the other, the piston ring will approach, overlap, and move away from each coil on the two interdigital electrodes, repeating the 4 stages shown in Figure 2(a). Each time the piston ring passes through a coil, a wave crest is generated. The movement range of the piston is covered by 11 pairs of coils on the cylinder, thus I_{sc} presents 11 alternating fluctuations during one piston stroke. And the amplitude of these I_{sc} peaks is linearly related to the instantaneous piston speed.

The expression for the instantaneous piston speed v_p in terms of the crank angle θ can be derived as Equation 3:

$$v_p = \frac{dx}{dt} = r\omega\left(sin\,\theta + \frac{\lambda\, sin\, 2\theta}{2}\right) = r\frac{2\pi n}{60}\left(sin\,\theta + \frac{\lambda\, sin\, 2}{2}\right) = \frac{\pi}{2}v_m\left(sin\,\theta + \frac{\lambda\, sin}{2}\right) \quad (3)$$

Substitute Equation 3 into Equation 2 to get Equation 4:

$$I_{sc} = \frac{dQ}{dx}v_p = \frac{dQ}{dx}\frac{\pi}{2}v_m\left(sin\,\theta + \frac{\lambda\, sin\, 2}{2}\right) \quad (4)$$

where dx: derivative of instantaneous piston position;

dt: time derivative;

r: crank radius;

l: connecting rod length;

ω: angular speed, $\omega = \frac{2\pi n}{60}$;

n: rotating speed of motor;

λ: the ratio of crank radius to connecting rod length, $\lambda = \frac{r}{l}$;

θ: crank angle;

v_m: mean piston speed, $v_m = \frac{2Sn}{60}$;

S: piston stroke, S=2r.

It can be seen that the I_{sc} changes periodically with the crank angle θ, and its peak value depends on the mean piston speed v_m.

To study the influence of the piston ring number on the output linearity and to confirm the rationality of the modular design, experiments with variable ring numbers and variable v_m are conducted. Figure 3(d) shows the RMS result of the I_{sc} measured from the PCTN equipped with 1, 2 and 3 rings respectively under different v_m. It can be seen that at the same speed condition, the RMS value of I_{sc} increases as the number of rings increases. As the v_m increases, the I_{sc}

RMS values corresponding to different ring numbers all show a linear increasing trend. Because as the number of rings increases, the contact area between the rings and the cylinder increases, which generates more charges and leads to a greater I_{sc}. It can be concluded that the I_{sc} is linearly related to the number of rings, indicating that the modular design allows multiple rings to well contact with the inner surface of the cylinder.

As shown in Figure 3(e), the material of the piston ring has a great influence on the I_{sc} at different v_m. Photographs of piston rings with different materials are shown in Supplementary **Figure S2**. The cylinder is made of PMMA material. When the material of the piston ring is POM, the linearity of the I_{sc} is the best and its slope with the increase of v_m is the largest. When polyether ether ketone (PEEK) is selected as the piston ring material, the linearity of I_{sc} is also acceptable. Compared with POM, the slope of PEEK's I_{sc} is lower, which is related to the affinity of the material to electrons. When the piston ring is made of other materials, I_{sc} remains at a low level throughout the entire speed range and its linearity is poor. This may be attributed to the difference in elastic properties of materials. The piston ring with poor elasticity cannot fit the cylinder well, resulting in a reduction in the contact area, which in turn leads to a reduction in charges and I_{sc}. Moreover, changes in tribo-dynamics caused by differences in material properties, such as stick-slip and distortions,[33] will reduce the effective contact area between the contact surfaces, thereby weakening the linear relationship between I_{sc} and v_m.

Next, the influence of cylinder materials on I_{sc} is experimentally investigated. Photographs of cylinders with different materials are shown in Supplementary **Figure S3**. Figure 3(f) shows the RMS value of I_{sc} for different cylinder materials with the ring material is POM. When the material of the cylinder is PMMA, the I_{sc} has the highest RMS value and the largest slope. When the cylinder is made of glass, the I_{sc} is lower than that of the PMMA material throughout the entire speed range, but its linearity is excellent. Compared with the above two materials, the I_{sc} corresponding to the PET cylinder is the lowest, and its linearity with the v_m has a certain degree of deterioration at high speeds. It can be concluded that the materials of the piston ring and the cylinder both have a significant effect on the I_{sc}. The above comparison shows that the combination of PMMA cylinder and POM piston ring has the best combined output characteristics.

2.4. Condition monitoring capability of the PCTN

The PCTN has a condition monitoring capability for piston rings and interdigital electrodes. Considering that the faults of the above two components can weaken the powering capacity of PCTN, identifying specific fault type is of great significance for guiding the maintenance of

reciprocating systems. For this reason, two types of abnormal conditions, piston ring missing and coil fracture, have been experimentally investigated. **Figure 4**(a) shows three fault cases of ring missing (case 1-3). Figure 4(b) shows 4 fault cases with different fracture positions and numbers (case 4-7).

The I_{sc} of two cases with one ring missing (case 1 and case 2) are close to each other, which is because the effective contact area between rings and cylinder is the same in both case. Figure 4(c) shows the time-domain waveform of I_{sc} under different ring missing faults and normal condition (3 rings). Under the same v_m condition, the I_{sc} waveform of all ring missing faults is similar to that of normal condition, but the amplitude of I_{sc} decreases as the number of missing rings increases. Figure 4(d) and (e) show the peak and RMS values of the I_{sc} for the normal condition and three fault cases. It can be seen that both the peak and RMS values decrease significantly as the number of piston rings decreases. The I_{sc} of two cases with one ring missing (case 1 and case 2) are close to each other, which is because the effective contact area between rings and cylinder is the same in both cases. This makes it difficult to locate the missing ring based on the above indicators of I_{sc}. For the case of two rings missing (case 3), the linearity of two indicators with the increase in v_m becomes worse, which is due to the deterioration of the concentricity between ring and cylinder caused by the excessive missing rings. In actual operation, the ring missing is one of the most serious faults. When any ring fails, the mechanical system needs to be shut down immediately for maintenance. Therefore, the condition monitoring of the piston ring based on I_{sc} is acceptable and sufficient to guide equipment maintenance.

The coil fracture on the interdigital electrode can also affect the I_{sc}. As shown in Figure 4(f) and (h), as the number of fractured coils increases, the peak and RMS values decrease, and the slope differ slightly. The decrease in I_{sc} is due to the decrease in the charges flowing through the circuit caused by the defect of coils. Continuous fractures of the coils, as in case 6, can deteriorate the linearity of I_{sc} with the v_m. The coil fracture at different positions of electrode can cause difference in the I_{sc} amplitude. Compared to the far-end fracture (case 5), the I_{sc} of PCTN with one coil fracture in the middle of electrode (case 4) is slightly lower. This is because more charges generated in the middle stroke cannot be transferred through the fractured coil, resulting in greater reduction in I_{sc}. Peak and RMS values of I_{sc} can be used to detect the coil fracture faults, but it cannot be used to accurately identify the location of faults. To this end, it is necessary to explore methods for locating the fractured coil based on time-domain analysis and time-frequency analysis.

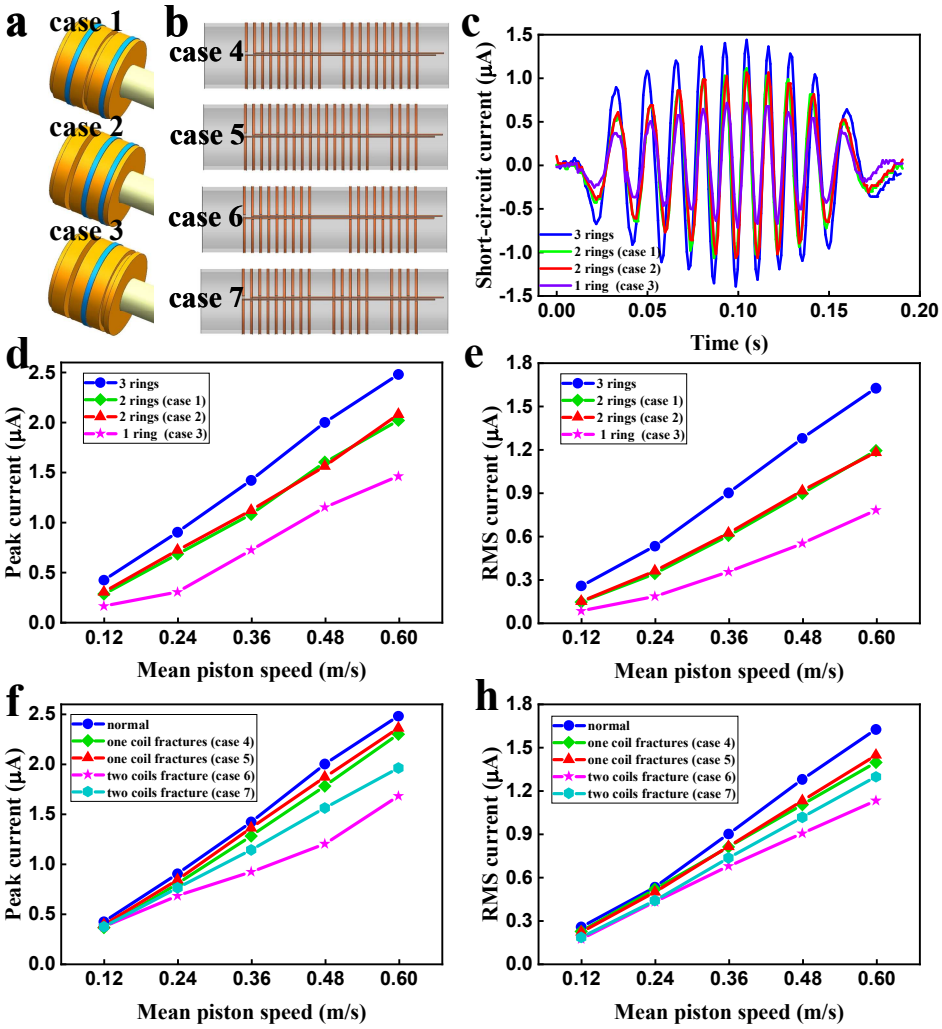

Figure 4. Condition monitoring capability of PCTN: Schematic diagram of (a) piston ring missing fault cases (case 1-3) and (b) coil fracture fault cases (case 4-7), (c) time-domain waveform, (d) RMS value, and (e) peak value of I_{sc} under different ring missing fault cases, (f) peak value and (h) RMS value of I_{sc} under different coil fracture fault cases.

Coil fracture can cause significant changes in the peak value of I_{sc} at a specific phase in time-domain waveform. **Figure 5** shows the measured I_{sc} time-domain signal of PCTN with coil fracture in the middle of electrode and equipped with one piston ring. Referring to the principle described in Figure 2(a), as the ring moves from electrode A to electrode B, negative charges flow from electrode B to electrode A, and the current direction is positive. When the ring is in position ①, with the coils B_0 and A_1 close to it are intact, the I_{sc} waveform is consistent with the normal case. Due to the fracture of the coils B_1 and A_2, when the ring moves to positions ②, ③ and ④, the induced charges can only be transmitted through the coils A_1 and B_2 that are far apart, resulting in an extension of alternating period. Moreover, the coils that are far apart weaken the electric field, so that the peak value of I_{sc} is reduced. It is important to note that the direction of I_{sc} with coil fracture at position ③ is opposite to that under normal condition.

This is because when the coils B_1 and A_2 are present, the direction of negative charges flow (from A_2 to B_1) is opposite to the direction (from B_2 to A_1) in the fault case. When the piston ring moves to position ⑤, the charges flow through the external circuit between coils B_2 and A_3, and the I_{sc} waveform again coincides with the curve of normal condition.

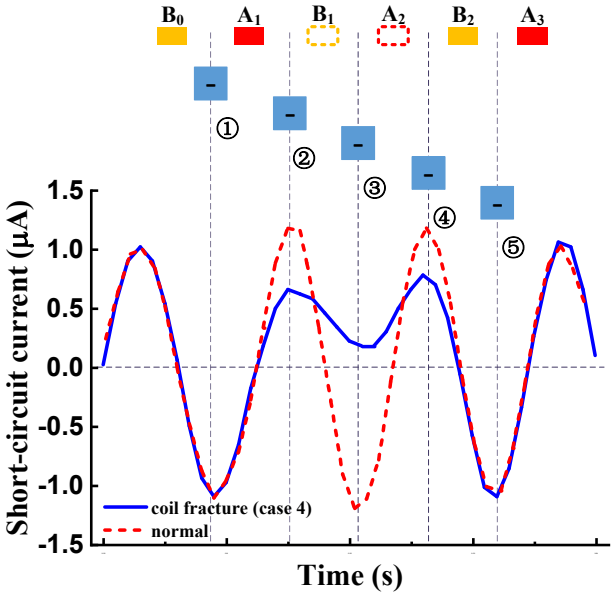

Figure 5. I_{sc} signals of PCTN with coil fractured and under normal conditions. The blue squares indicate the piston ring at different moments, and the red and orange rectangles represent the coils on different interdigital electrodes, where the hollow rectangles represent the fractured coils.

Figure 6 shows the I_{sc} signal in time-domain of a PCTN equipped with different numbers of piston rings and coil fracture at different positions. The different rows show the I_{sc} signals corresponding to different ring arrangements, and the different columns correspond to two fault cases (case 4 and case 5) with coil fractured at different positions.

As shown in Figure 6(a), for the PCTN equipped with one ring, the coil fracture in the middle of electrode caused the reduction of one peak (①) in the I_{sc} curve. When the PCTN is equipped with two rings, the change in I_{sc} curve caused by the coil fracture is different, referring to different ring arrangement. As shown in Figure 6(b), when there is one missing ring between the two rings, the peaks on both sides of one normal peak (① and ②) on the I_{sc} curve are significantly reduced. This is because when the ring missing position is aligned with the fractured coils, both normal rings are close to the intact coil, causing the peak at the middle position to return to normal. When the piston rings are arranged adjacent to each other, as shown in Figure 6(c), the coil facture leads to a reduction in the two adjacent peaks (① and ②) of I_{sc}. It can be seen that when the coil fracture and the ring missing fault occur at the same time, the

location of the ring missing can be identified based on the difference in the I_{sc} waveform. With the increase in the number of rings, the number of peak reductions caused by coil fracture increased, but the reduction degree of I_{sc} peaks decreased significantly. As shown in Figure 6(d), when three rings are installed, there are three peaks (①, ②, and ③) decrease, and the reduction is smaller than that of two rings. Comparing the left and right columns, it can be seen that the I_{sc} waveform showed a significant drop in amplitude at specific phase corresponding to the location of coil fracture. This correspondence can be used to locate the position of coil fracture based on time-domain signals.

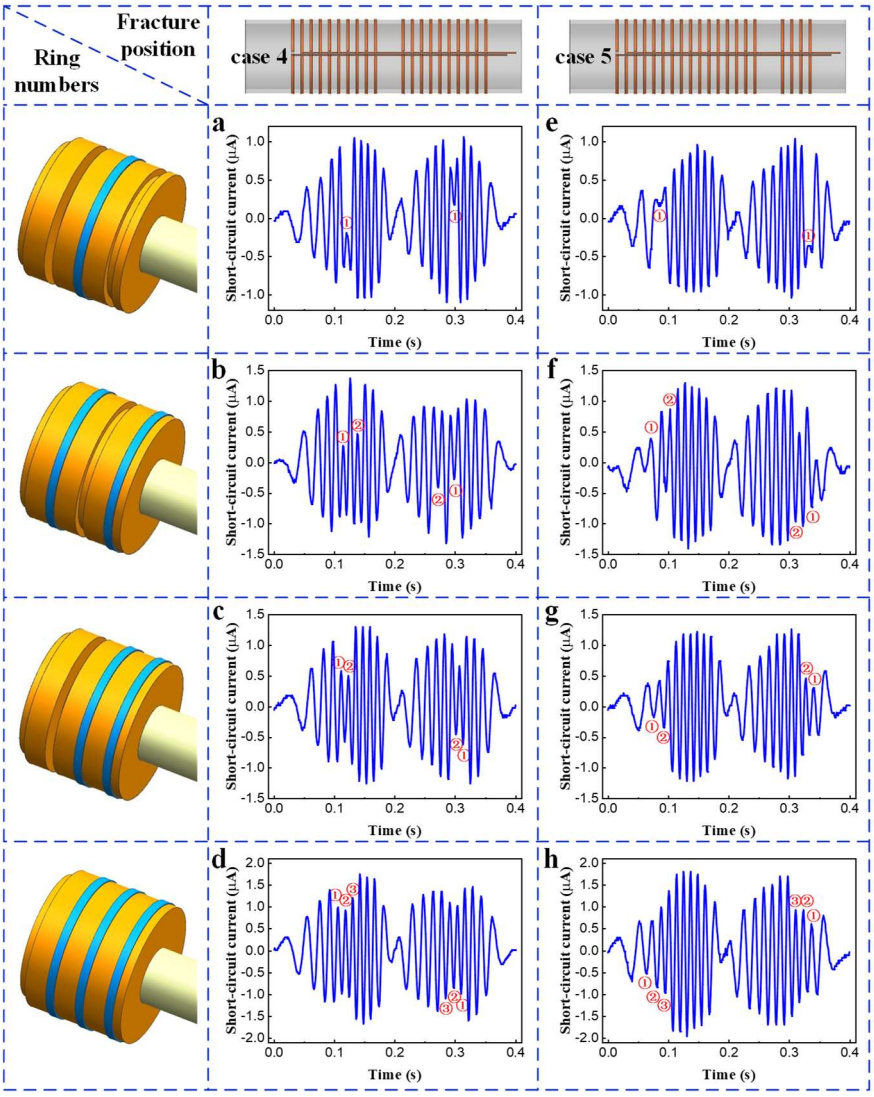

Figure 6. I_{sc} signals in time-domain of PCTN equipped with different numbers of piston rings and coil fracture at different positions. Coils fractured in the middle of cylinder (case 4) with (a) one piston ring, (b-c) two piston rings, and (d) three piston rings. Coils fractured at the far-end of cylinder (case 5) with (e) one piston ring, (f-g) two piston rings, and (h) three piston rings.

It is known from Figure 5 that the coil fracture fault will not only cause the reduction of

peaks in I_{sc} signal, but may also cause extension of specific alternating period, that is, the reduction of the response frequency. Then the coil fracture faults in PCTN are identified and located by time-frequency analysis. **Figure 7** shows short-time Fourier transform (STFT) results of I_{sc} measured in normal condition and two fault cases with coil fractured at different positions. For more clarification in understanding the STFT result, the raw I_{sc} signals are presented alongside of STFT. As shown in Figure 7(a), the STFT spectrum of I_{sc} measured in normal condition shows continuous inverted V-shaped patterns in one operating cycle. The frequency of I_{sc} increases first and then decreases, reaching the maximum in the middle of the stroke, which is consistent with the change of instantaneous piston speed. The occurrence of coil fracture will cause discontinuity in this inverted V-shaped pattern. When the coil in the middle of the coil fractures (case 4), the inverted V-shaped pattern in the STFT spectrum appears discontinuous in the middle, as marked with a black dashed box in Figure 7(b). Moreover, a low-frequency component whose frequency is close to half of the original frequency component appears in the phase corresponding to the coil fracture, as marked with a red dashed box. As explained in Figure 5, this low-frequency feature is caused by the decrease in the number of current reversals. When the coil at the far end of the coil fractures (case 5), the fault features in the STFT spectrum are more distinct, as shown in Figure 7 (c). This is because the piston speed decreases as it approaches the end of the cylinder, resulting in a significant reduction in the charges flowing through the adjacent coils of the fractured coils and the discontinuity effect is more obvious. It can be concluded that coil fracture faults can be accurately identified and located through time-frequency analysis.

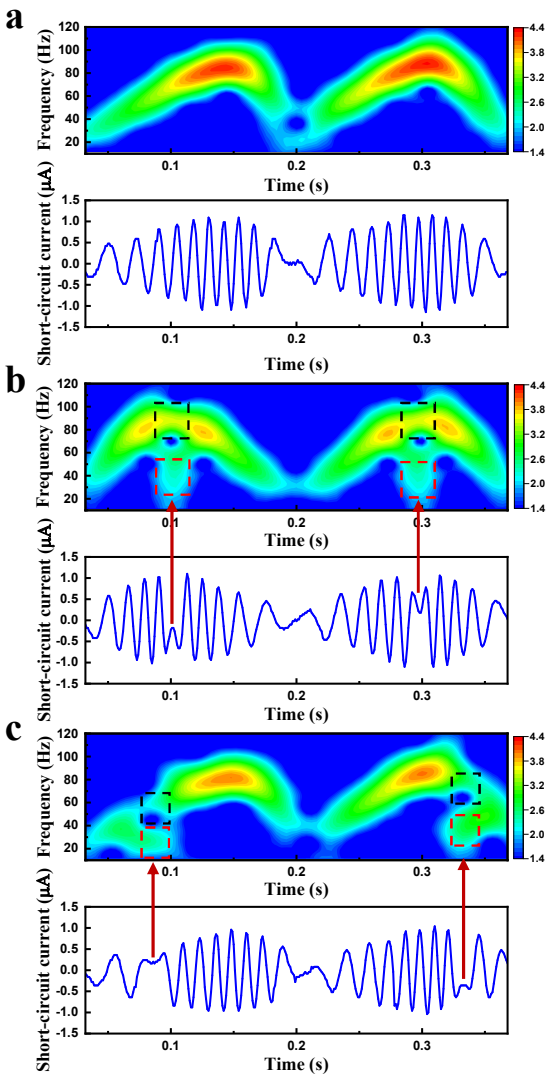

Figure 7. Time-frequency representation of I_{sc} measured from a PCTN equiped with one piston ring and operated at v_m=0.36 m s^{-1}, (a) under normal condition, (b) with coil fractured in the middle of interdigital electrode and (c) with coil fractured at the far end of the interdigital electrode.

3. Conclusion

In summary, a piston-cylinder triboelectric nanogenerator (PCTN) is proposed based on the lateral sliding mode of the TENG, and the PCTN designed has condition monitoring and self-powering capabilities. The short-circuit current (I_{sc}) and open-circuit voltage (V_{oc}) at different mean piston speed (v_m) are measured and analysed. Since the interdigital electrodes can be regarded as a capacitor with a constant capacitance, the V_{oc} will not change significantly with the v_m. While the peak and RMS values of I_{sc} have a good linear relationship with the v_m, which are regarded as the key characteristic parameters of PCTN. The more piston rings equipped in the PCTN, the greater the values of I_{sc}. The materials of the piston ring and cylinder

all have significant effects on the I_{sc}. In this work, a PCTN with PMMA cylinder and POM piston rings has the best powering performance. The PCTN has excellent monitoring and diagnosis capabilities for piston ring missing and coil fracture faults. Piston ring missing faults can be effectively identified based on the variations in peak and RMS values of I_{sc}. And coil fracture faults can be identified and located by analyzing changes in time-domain curve and time-frequency spectrum of I_{sc}. This work proposes a device with condition monitoring and self-powering capabilities, which has widespread application prospects in operation monitoring and maintenance guidance of reciprocating devices.

4. Experimental Section

The piston rings with different materials (POM, FEP, PET, PEEK, PP, and PTFE) have been polished and cleaned to ensure close contact with the inner wall of the cylinder. Then the piston ring was cut according to the circumference of the inner wall of the cylinder. The interdigital electrodes were made of a thin copper sheet with a thickness of 0.05 mm and were pasted to the outer surface of the cylinder using conductive silver paint. Finally, the piston assembly was installed inside the cylinder and the PCTN fabrication was completed. The test rig is composed of an AC motor (5RK120RGU-CF, 120W, 1350r/min), a reducer, a frequency converter, a crank-link mechanism, a Hall sensor, a speed indicator, a pedestal and a PCTN. The reducer was installed behind the motor to reduce drive speed and increase torque.

The open-circuit voltage of the PCTN is measured using a TDS2024C oscilloscope. The short-circuit current is converted into voltage output using a trans-impedance amplifier.

Supporting Information

Supporting Information is available from the Wiley Online Library or from the author.

Acknowledgements

This work was sponsored by the Natural and Scientific foundation of China NO. 51805353 and Research Project Supported by Shanxi Scholarship Council of China NO. HGKY2019041. Thanks to Tiantian Yang, Chaoliang He, Hang Bian and Senxiang Li, of Taiyuan University of Technology, for their help in experimental testing.

Received: ((will be filled in by the editorial staff))
Revised: ((will be filled in by the editorial staff))
Published online: ((will be filled in by the editorial staff))

References

[1] J. Chen, R. B. Randall, B. Peeters, *Mechanical Systems and Signal Processing* **2016**, *75*, 434.

[2] K. L. P Tharanga, S. Liu, S. Zhang, Y. Wang, Z. *Angew. Math. Phys.* **2020**, *8*, 2031.

[3] D. Ning, C. Sun, Y. Gong, Z. Zhang, J. Hou, *Mechanical Systems and Signal Processing* **2016**, *75*, 544.

[4] Z. Wang, W. Wu, *Angew. Chem., Int. Ed.* **2012**, *51*, 11700.

[5] Z. Wang, *Faraday Discuss.* **2014**, *176*, 447.

[6] C. Wu, A. C. Wang, W. Ding, H. Guo, Z. Wang, *Adv. Energy Mater.* **2019**, *9*, 1802906.

[7] Z. Wang, *ACS Nano* **2013**, *7*, 9533.

[8] W. Yang, X. Wang, P. Chen, Y. Hu, L. Li, Z. Sun, *Nano Energy* **2021**, *85*, 106037.

[9] H. Lin, Y. Liu, S. Chen, Q. Xu, S. Wang, T. Hu, P. Pan, Y. Wang, Y. Zhang, N. Li, Y. Li, Y. Ma, Y, Xie, L. Wang, *Nano Energy* **2019**, *65*, 103944.

[10] Q. Jing, G. Zhu, P. Bai, Y. Xie, J. Chen, R. P. S. Han, Z. Wang, *ACS Nano* **2014**, *8*, 3836.

[11] G. Zhu, J. Chen, Y. Liu, P. Bai, Y. S. Zhou, Q. Jing, C. Pan, Z. Wang, *Nano Lett.* **2013**, *13*, 2282.

[12] W. Choi, I. Yun, J. Jeung, Y. S. Park, S. Cho, D. W. Kim, I. S. Kang, Y. Chung, U. Jeong, *Nano Energy* **2019**, *56*, 347.

[13] Y. Han, W. Wang, J. Zou, Z. Li, X. Cao, S. Xu, *Nano Energy* **2020**,*76*, 105008.

[14] S. Xu, Y. Feng, Y. Liu, Z. Wu, Z. Zhang, M. Feng, S. Zhang, G. Sun, D. Wang, *Nano Energy* **2021**, 85, 106023.

[15] S. Niu, Y. Liu, X. Chen, S. Wang, Y. S. Zhou, L. Lin, Y. Xie, Z. Wang, *Nano Energy* **2015**, *12*, 760.

[16] Z. Zhang, Y. Bai, L. Xu, M. Zhao, M. Shi, Z. Wang, X. Lu, *Nano Energy* **2019**, *66*, 104169.

[17] L. Lin, Y. Xie, S. Niu, S. Wang, P. Yang, Z. Wang, *ACS Nano* **2015**, *9*, 922.

[18] X. Zhang, M. Han, R. Wang, B. Meng, F. Zhu, X. Sun, W. Hu, W. Wang, Z. Li, H. Zhang, *Nano Energy* **2014**, *4*, 123.

[19] M. Xu, T. Zhao, C. Wang, S. L. Zhang, Z. Li, X. Pan, Z. Wang, *ACS Nano* **2019**, *13*, 1932.

[20] L. Xu, T. Jiang, P. Lin, J. J. Shao, C. He, W. Zhong, X. Y. Chen, Z. Wang, *ACS Nano* **2018**, *12*, 1849.

[21] M. He, W. Du, Y. Feng, S. Li, W. Wang, X. Zhang, A. Yu, L. Wan, J. Zhai, *Nano Energy* **2021**, *86*, 106058.

[22] H. Liu, H. Wang, Y. Lyu, C. He, Z. Liu, *Microelectron. Eng.* **2020**, *224*, 111231.

[23] Z. Zhang, J. He, T. Wen, C. Zhai, J. Han, J. Mu, W. Jia, B. Zhang, W. Zhang, X. Chou, C. Xue, *Nano Energy* **2017**, *33*, 88.

[24] H. Yu, X. He, W. Ding, Y. Hu, D. Yang, S. Lu, C. Wu, H. Zou, R. Liu, C. Lu, Z. Wang, *Adv. Energy Mater.* **2017**, *7*, 1700565.

[25] C. Xiang, C, Liu, C. Hao, Z. Wang, L. Che, X. Zhou, *Nano Energy* **2017**, *31*, 469.

[26] Y. Ren, G. Liu, H. Yang, T. Tong, S. Xu, L. Zhang, J. Luo, C. Zhang, G. Xie, *Nano Energy* **2020**, *68*, 104303.

[27] J. Wang, W. Ding, L. Pan, C. Wu, H. Yu, L. Yang, R. Liao, Z. Wang, *ACS Nano* **2018**, *12*, 3954.

[28] Q. Xu, Y. Lu, S. Zhao, N. Hu, Y. Jiang, H. Li, Y. Wang, H. Gao, Y. Li, M. Yuan, L. Chu, J. Li, Y. Xie, *Nano Energy* **2021**, *89*, 106382.

[29] Q. Shi, H. Wang, T. Wang, C. Lee, *Nano Energy* **2016**, *30*, 450.

[30] S. Jeon, Y. Nho, S. Park, W. Kim, I. Tcho, D. Kim, D. Kwon, Y. Choi, *Nano Energy* **2017**, *41*, 139.

[31] Q. Xu, Y. Fang, Q. Jing, N. Hu, K. Lin, Y. Pan, L. Xu, H. Gao, M. Yuan, L. Chu, Y. Ma, Y. Xie, J. Chen, L. Wang, *Biosens. Bioelectron.* **2021**, *187*, 113329.

[32] Q. Han, Z. Ding, Z. Qin, T. Wang, X. Xu, F. Chu, *Nano Energy* **2020**, *67*, 104277.

[33] Z. Luo, B. Song, J. Han, S. Yan, *Chin. Phys. B* **2019**, *28*, 104601.